1   Revised version 1

2

3   Octahedral chemistry of 2:1 clay minerals and hydroxyl band position in the near-infrared.

4   Application to Mars.

5

6

7

8

9   Javier Cuadros[a],*, Joe R. Michalski[a], Vesselin Dekov[b], Janice L. Bishop[c]

10

11

12   [a] Natural History Museum, Department of Earth Sciences, Cromwell Road, London SW7 5BD

13   [b] Laboratoire de Géochimie et Métallogénie, Département Géosciences Marines, IFREMER, Z.I.
14   Pointe du diable, BP 70 – 29280 Plouzané, France

15   [c] SETI Institute, Mountain View, CA 94043, USA

16

17

18

19   Short title: Octahedral chemistry and NIR analysis of martian clays.

20

21

22   * Corresponding author. Tel.: +44 20 7942 5543; fax: +44 20 7942 5537

23   E-mail address: j.cuadros@nhm.ac.uk

24

25

26

Abstract

27

28   With the arrival of Curiosity on Mars, the MSL has started its ground validation of some of the

29   phyllosilicate characterization carried out with remote sensing near-IR spectroscopy from orbital

30   instruments. However, given the limited range of action of the rover, phyllosilicate identification and

31   characterization will have to rely mainly on orbital near-IR data. Investigation of Earth analogues

32   can greatly assist interpretation of Martian spectra and enable more robust analyses. In this

33   contribution, Mg/Fe-rich clays from submarine hydrothermal origin that had been thoroughly

34   characterized previously were investigated with near-IR reflectance spectroscopy. The clays are

35   mixed-layer glauconite-nontronite, talc-nontronite, talc-saponite and nontronite samples. The

36   hydroxyl bands in the range 2.1-2.35 μm were decomposed into their several individual

37   components to investigate correlations between the octahedral chemistry of the samples and the

38   normalized intensity of several bands. Good correlations were found for the samples of exclusive

39   dioctahedral character (glauconite-nontronite and nontronite), whereas poor or no correlations

40   emerged for the samples with one (talc-nontronite) or two (talc-saponite) trioctahedral layer

41   components, indicating a more complex spectral response. Because these bands analyzed are a

42   combination of the fundamental OH stretching and OH bending vibrations, the response of these

43   fundamental bands to octahedral chemistry was considered. For 2:1 dioctahedral phyllosilicates,

44   Fe and Mg substitution for Al displaces both fundamental bands to lower wavenumbers (longer

45   wavelenghts), so that their effect on the position of the combination band is coherent. In contrast,

46   for trioctahedral clays, Al and Fe^{3+} substitution of octahedral Mg displaces the OH stretching band

47   to lower wavenumber values, and the OH bending band to higher wavenumber values, resulting in

48   partial or total mutual cancelation of their effects. As a result, clays with near-IR spectra indicating

49   Mg-dominated octahedral compositions may in fact contain abundant Fe and some Al substitution.

50   Thus, remote-sensing near-IR mineralogical and chemical identification of clays on Mars appears

51   relatively straightforward for dioctahedral clay minerals but more problematic for trioctahedral

52   clays, for which it may require a more detailed investigation of their near-IR spectra.

53

54   Keywords: Infrared observations; Mars; Mineralogy.

55

Introduction

57 Recent exploration of Mars using near-infrared (NIR) reflectance spectroscopy has produced one

58 of the most important discoveries in Planetary Science, and one which is generating unabated

59 interest (e.g., Bibring et al., 2006; Vaniman et al., 2014). Data from the MEx/OMEGA (Mars

60 Express Observatoire pour la Minéralogie, l'Eau, les Glaces et l'Activité) and MRO/CRISM (Mars

61 Reconnaissance Orbiter Compact Reconnaissance Imaging Spectrometer for Mars) instruments

62 have revealed thousands of exposures of phyllosilicate-rich rocks within the Martian crust (Poulet

63 et al., 2005; Murchie et al., 2009; Ehlmann et al., 2011a; Carter et al., 2013). Data from the rover

64 Curiosity have allowed the identification of clay in fluvio-lacustrine materials on the floor of Gale

65 Crater (Vaniman et al., 2014; Bristow et al., 2015), and the rover Opportunity provided information

66 that helped to characterize a clay-bearing suite at Endeavour Crater (Arvidson et al., 2014). Most

67 of the deposits correspond to ancient (Noachian-age, 3.7-4.3 Ga), layered bedrock, most often

68 exposed in impact craters (Ehlmann et al., 2011a; Carter et al., 2013). While geomorphic evidence

69 has long suggested the presence of water on ancient Mars, at least during brief episodes (Carr,

70 1996), the unambiguous detection of phyllosilicates (Poulet et al., 2005) is the first clear evidence

71 for sustained aqueous activity (Bibring et al., 2005). Furthermore, they seemingly date to the same

72 period when life was forming or beginning to take hold on Earth. Considering that (1) phyllosilicates

73 are among the best materials for preserving evidence of life (Walter & Des Marais, 1993) and (2)

74 microbial activity on Earth promotes phyllosilicate formation (Douglas and Beveridge, 1998) and

75 acts as a modifier of phyllosilicate composition (Cuadros et al., 2013a), Martian clays are very

76 important astrobiological targets. Beyond the possible link to life, Martian clays are important

77 because they provide information about hydrous processes that took place on Mars, such as the

78 water chemistry, water-to-rock ratio, and temperature.

79

80 So far, the chemical and mineralogical characterization of Martian phyllosilicates has been mainly

81 based on NIR spectroscopy. The three main features in NIR spectra used for this purpose are the

82 absorption bands at ~1.4 and 2.18-2.35 μm, corresponding to hydroxyl vibrations, and at ~1.9 μm

83 corresponding to molecular water vibrations. There are also vibrations of molecular water of lower

84 intensity in the range 1.41-1.45 μm (Bishop et al., 1994). The hydroxyl bands (~1.4, 2.18-2.35 μm)

85   change their position depending (mainly) on the chemistry of the octahedral sheet within the

86   phyllosilicate layers (e.g., Bishop et al., 2008). The existence of hydration water (band at ~1.9 μm)

87   is frequently interpreted as indicative of smectite. Other features such as two wide crystal-field

88   absorption bands in the 0.6-1.3 μm region indicate significant Fe content (e.g., Burns, 1993), an

89   obvious band at ~2.4 μm is associated with large Fe and/or Mg content (Michalski et al, 2014) but

90   not exclusively, and doublets or multiplets at the ~1.4 and 2.18-2.35 μm regions are indicative of

91   kaolinite, talc or serpentines, depending on the specific position (Bishop et al., 2002b; Zhang et al.,

92   2006). Saponite, halloysite and sepiolite also display or can display multiplets in these regions

93   (Carter et al., 2013; Robertson and Milliken, 2014), typically less resolved and with less diagnostic

94   value. Carter et al. (2013) have compiled the several clay minerals identified on Mars in the

95   following order of frequency: Fe-Mg phyllosilicates (most of them interpreted as smectite) >>

96   chlorite and corrensite > Al-smectite and Al-mica > kaolin (typically interpreted as kaolinite) >

97   serpentines.

98

99   The identification and characterization of clay minerals on Mars at a global scale will continue

100   relying heavily on NIR remote sensing, as the operation radius of present and future probes is

101   limited. It is then necessary to progress in our ability to read the crystal-chemical character of

102   Martian clays from their NIR spectra, work that can be carried out by careful characterization of

103   Earth analogues and comparison with Martian counterparts. Such is the context of recent studies

104   on kaolinite-smectite mixed-layer (Cuadros and Michalski, 2013), beidellite-montmorillonite series

105   (Bishop et al., 2011), mixtures of Al-rich clays and rhyolitic glass (McKeown et al, 2011), and

106   Fe/Mg-rich clays (Cuadros et al., 2013b). The present contribution uses this same strategy.

107   Crystal-chemical characteristics of a set of well-characterized Fe/Mg-rich clays of submarine

108   hydrothermal origin (Cuadros et al., 2013b) are correlated with their NIR features in order to gain

109   insights that allow a more accurate identification of Martian clays. Clays of Fe/Mg composition are

110   of great relevance to Mars because they comprise by far the most abundant phyllosilicate

111   detections from orbital observation (Carter et al., 2013).

112

Materials and methods

114   Cuadros et al. (2013b) describe in detail the investigated clays, their location of origin and their

115   formation environment. They are from seafloor hydrothermal fields in the Atlantis II Deep (Red

116   Sea), Guaymas Basin (Gulf of California), Grimsey Graben (Tjörnes Fracture Zone; off the

117   Icelandic north coast), East Pacific Rise, and Mid-Atlantic Ridge. They comprise four groups,

118   glauconite-nontronite (G-N) mixed-layer clays, nontronite, talc-nontronite (T-N) and talc-saponite

119   (T-S). Two other samples of terrigenous origin were included for comparison. They are Nontronite

120   33B, a nontronite product of hydrothermal alteration of the Columbia River Basalt (Manito,

121   Spokane County, Washington, USA), and Nontronite 51, which is in fact a mixture of nontronite

122   (75%) and T-N (95% T, 5% N) from unknown origin and location. Chemical and Mössbauer

123   analyses of these samples, their results and the transformation of the data into the structural

124   formulas of the clays are described by Cuadros et al. (2013b). Here, the octahedral composition of

125   the clays is reported (Table 1).

126

127   For the complete description of sample preparation refer to Cuadros et al. (2013b). Before the

128   study described here, samples were ground manually in an agate mortar until a fine, homogeneous

129   powder was obtained. These powders were analyzed using NIR spectroscopy in reflectance mode

130   at RELAB (Reflectance Experiment Laboratory, Brown University, Rhode Island, USA). Two sets of

131   conditions were used: analysis of the 0.33-2.54 μm range at a resolution of 0.01 μm, with an UV-

132   VIS-NIR bidirectional spectrometer; and a more detailed analysis of the region 2.15-2.40 μm at a

133   resolution of 2 cm^{-1} with a Thermo Nexus 870 FTIR. The second, detailed analysis was not carried

134   out for the specimens labelled POS (Tables 1 and 2) due to lack of sample. The samples were

135   investigated as powder against pressed halon (0.33-2.54 μm) and a brushed gold reference (2.15-

136   2.40 μm), in ambient air atmosphere. In these conditions all samples had their smectite layers

137   hydrated. This is proven because there is a good positive correlation ($R^2 = 0.72$) between hydration

138   water loss (thermogravimetry; water loss < 200 C) and proportion of smectite layers (XRD) in the

139   samples (Cuadros et al., 2013b).

140

141   The spectra, consisting of reflectance versus wavelength values, were analyzed using the

142   Grams/AI software package from Thermo Galactic. The bands in the range 2.15-2.40 μm,

143   corresponding to one of the OH absorption bands, were investigated. First the curved background

144   was transformed into a straight, continuum-removed baseline by fitting a quartic or quintic function

145   to the continuum and subtracting it from the spectrum. The spectrum was then deconvolved by

146   Fourier self-deconvolution to locate the position of the absorption maxima (appearing as minima in

147   the reflectance spectra). This procedure decreases bandwidths and resolves overlapping bands.

148   For each sample, the Fourier self-deconvolution was performed repeatedly using different

149   parameters and the selected result was based on two criteria, (1) the deconvolved spectra had a

150   set of well-resolved maxima that were reproduced consistently in the several calculations and (2)

151   artifact maxima (e.g., those generated on a flat area of the original spectrum) were absent. The

152   number of bands resolved with this technique varied between 1 and 6 (see results section). Finally,

153   the values of the band centers obtained from the deconvolution process were used to model the

154   individual absorption bands by curve-fitting, using Gaussian curves, as suggested for wavelength

155   space (Parente et al., 2011). After a first fit with the band center values from the deconvolution

156   process, the parameters (band positions, widths and heights) were left free to vary. In some cases

157   the position, height or width of one band had to be fixed to avoid producing results with no physical

158   meaning. The fixed parameters were guided by the results from the deconvolution process and by

159   fitting results from similar samples that were more straightforward to model. The areas of the

160   individual bands were normalized to the sums of all areas of the components attributed to OH

161   vibrations. We refer to these values hereafter as normalized bands or normalized intensities.

162

163   Some of the samples contained traces of carbonates (Cuadros et al., 2013b). Carbonates have

164   one band in the range 2.30-2.35 μm that might interfere with our study. Carbonate bands were

165   detectable by small peaks in the mid-IR at ~1400 cm^{-1} and, in some cases, by small bands or

166   shoulders at ~870 cm^{-1} (analyses in the mid-IR in reflectance and transmission mode in support of

167   the data presented in this contribution). However, the carbonate bands at 3.4 and 3.9 μm, of lower

168   intensity than the above features, are not observable in any of the samples. The carbonate band at

169   ~2.3 μm, is ~10 times less intense than those at 3.4 and 3.9 μm and thus we can conclude that

170   there is no interference of carbonate vibrations in our study. Other samples contained traces of

171   sulphates, which may produce bands in the region 2.2-2.3 μm. The possibility that these bands

172   were present in our samples was assessed checking for sulphate bands at ~1200 cm^{-1} in the mid-

173   IR. Only one case showed a mid-IR sulphate band indicating the possibility that there is some

174   sulphate interference. Finally, hydrated silica may have also caused interference in one sample in

175   the range 2.2-2.3 μm, where opal has an intense and wide absorption band. These cases are

176   discussed in the results section.

177

178   **Results**

179   The NIR spectra displayed variable band depth (i.e., band "height": distance from baseline to

180   peak), very low for some of them (Va3-382-389, Va3-150-153). There is no obvious reason for this

181   difference. It may be due to the presence of pyrite, hematite or some other phases present in minor

182   amounts (Cuadros et al., 2013b), or it may be caused by some physical characteristic of the clay

183   particles in relation with their origin, such as particle roughness, shape or dimensions. The spectra

184   showed clearly the OH band at ~2.3 μm, indicating their Fe/Mg-rich character, and the molecular

185   water band at ~1.9 μm. However, the OH absorption band at ~1.4 μm had highly variable intensity

186   and is frequently almost imperceptible. All the spectra displayed one or two wide crystal-field

187   absorption bands of different shape and depth in the 0.6-1.3 μm region, indicating the presence of

188   Fe. A composite band in the range 2.35-2.4 μm was present, associated (but not exclusively) with

189   significant Fe and/or Mg content. For the spectra of samples containing talc, the ~2.3 μm band was

190   a doublet, where the two bands were resolved to a variable extent. The proportion of smectite

191   layers in T-N and T-S was one of the factors modifying the resolution of this doublet, generally

192   more resolved in talc-rich samples (see Fig. 1, samples Va22-575-577 and Sea Cliff Dive, with

193   71% and 27% smectite, respectively). However, crystal-chemical factors of the talc are also an

194   important control on the resolution of this doublet. For example, the specimen with the greatest

195   proportion of talc is 1183-9, a T-S with 98% talc layers, but its doublet is poorly resolved (Fig. 2).

196   This sample has a large octahedral Fe content (0.75 Fe^{3+} and 0.55 Fe^{2+} per $O_{10}[OH]_2$; Cuadros et

197 al 2013b) and poorly defined hkl XRD peaks, indicative of a crystal lattice with many structural

198 defects.

199

200 The decomposition of the peaks produced a variable number of underlying bands (Figure 2, Table

201 2). The most intense peaks were readily assigned from the known octahedral composition of the

202 clays. Smaller peaks were more difficult to assign, and we do it here (Table 2) only tentatively. For

203 these difficult assignments we balanced several arguments, such as band assignments in previous

204 studies, octahedral cation abundance in the samples and an approximate progression of

205 increasing wavelength of the M_2OH and M_3OH individual bands by substituting the following

206 cations into the group $Al^{3+} < Fe^{3+} < Mg^{2+} < Fe^{2+}$. In addition, it is possible that the most intense

207 peaks are generated by the overlap of two or more peaks representing different cation groups

208 around the hydroxyls. The analysis below and in the discussion section suggests that the location

209 of individual OH combination bands is controlled by more factors than simply the nature and

210 number of cations surrounding individual OH groups. Unless stated otherwise in the results below,

211 Fe in dioctahedral groups (two metal atoms next to an OH group) is Fe^{3+}, whereas Fe in

212 trioctahedral groups (three metal atoms linked to an OH group) is Fe^{2+}.

213

214 In the G-N samples, there is an intense band at ~2.29 μm that corresponds to Fe_2OH vibrations

215 and another at 2.31-2.32 μm, generally of lower intensity, that can be assigned to FeOHMg (Table

216 2). These assignments are in agreement with the octahedral composition of the samples (Table 1).

217 It is more difficult to assign the band at 2.27-2.28 μm that appears in two samples and the low

218 intensity bands at ~2.36 μm (Table 2). One possibility is that the 2.27-2.28 μm band corresponds

219 to Fe_2OH in nontronite layers, as is typically observed (Bishop et al., 2002b), and the band at ~2.29

220 μm is the same vibration in the glauconite layers. The obvious difficulty to this interpretation is that

221 there is no correlation between the proportion of nontronite layers and the area of the bands at

222 2.27-2.28 μm. These bands are probably related to more than one chemical factor. The small band

223 at ~2.36 μm can be assigned to Fe^{2+}_3OH groups. Mössbauer analysis of three of the G-N samples

224 did not display any Fe^{2+} (Table 1) but it is possible that there is some because the absolute

225   uncertainty of the integrated areas of doublet peaks determined using Mössbauer spectroscopy

226   was 3-5% (Cuadros et al., 2013b; each doublet peak representing Fe^{2+} and Fe^{3+} in a specific

227   chemical environment). The actual intensity of the possible Fe^{2+}_3OH band would not only depend

228   on the amount of Fe^{2+} present but on the cation ordering in the octahedral sheet, especially if Fe^{2+}

229   is in very low concentration. The assignment of the 2.27-2.28 and 2.36 μm bands is thus left

230   unresolved.

231

232   In the nontronite group the assignments are in good agreement with the chemistry of the samples.

233   Cy-82-14-5 and 1183-15 have Mg and no Al, and they display Fe_2OH (~2.28 μm) and FeMgOH

234   (~2.30 μm) bands. Cy-82-14-5 also displays a band at 2.329 μm possibly due to Mg_3OH or

235   Mg_2FeOH. Nontronite 33B has low Al and Mg abundances and there are two small bands that can

236   be assigned to Al_2OH (2.204 μm) and AlFeOH (2.239 μm). Alternatively, the latter, may correspond

237   to AlMgOH vibrations.

238

239   In the T-N group the main band is in the range 2.280-2.295 μm and assigned, in principle, to

240   Fe^{3+}_2OH, although the range is sufficiently wide to allow further discrimination. There are possible

241   FeMgOH, Mg_2FeOH and Mg_3OH bands of low intensity in only three of the samples (Table 2) and

242   thus, the significant amount of octahedral Mg in the T-N samples is not accounted for in the band

243   assignment. From their previous study, Cuadros et al. (2013b) concluded that the talc layers in the

244   T-N specimens from submarine hydrothermal sites had nontronite domains, i.e., there is an excess

245   of Fe^{3+} in the talc octahedral sheets. Even in this situation, the scarcity of FeMgOH and Mg_3OH

246   vibrations is difficult to explain. Possibly, the main band at 2.280-2.295 μm contains FeMgOH

247   vibrations. Finally, Nontronite 51 has bands that could correspond to Al_2OH and AlFeOH groups,

248   with the difficulty that no Al was assigned to the octahedral sheet of this sample (Table 1). This

249   discrepancy may be explained by the interference of hydrated silica, as ~9% silica was identified in

250   this sample (Cuadros et al., 2013b). Opal has a wide NIR band in the range 2.2-2.3 μm, modulated

251   to a variable extent into two maxima (McKewon et al., 2011; Ehlmann et al., 2011b), that might be

252   the cause of the low intensity bands at 2.203 and 2.243 μm in Nontronite 51 (Table 2).

253

254 The T-S group displays the talc Mg_3OH doublet at ~2.29 and ~2.31 μm. Other possible bands are

255 Fe_2OH at 2.264-2.283 μm, where the valence of the Fe atoms is left unspecified. Other small

256 bands can be assigned to AlMgOH and AlFeOH groups, with the difficulty that no or very little Al

257 was assigned to the octahedral sheet of these samples. In one case, Va3-382-389, the band at

258 2.195 μm, tentatively assigned to AlMg, could originate from sulphate trace (mirabilite,

259 $Na_2SO_4 \cdot 10H_2O$, was identified by Cuadros et al., 2013b). There are also two small bands at 2.352

260 μm that could correspond to either Mg_3OH or Fe^{+2}_3OH groups (Table 2). If corresponding to

261 Mg_3OH, they could be vibrations in saponite layers, rather than in talc layers.

262

263   **Discussion**

264 The above assignments show that the main features of the NIR spectra are consistent with the

265 mineralogy and chemistry of the samples, but there are small bands that cannot be easily

266 reconciled with them. The reasons for this discrepancy can be multiple. First of all, there are some

267 cases of uncertainty due to contamination. Then, clay minerals have a certain degree of chemical

268 heterogeneity between particles. This is true even of single-phase clay minerals. The structural

269 formula is an average composition of all particles. This means that the real clay contains grains or

270 chemical domains with small departures from the average octahedral composition in the structural

271 formula. If the phyllosilicate is a mixed-layer phase, the differences between the average structural

272 formula and the real crystal-chemical domains can become more important, because the

273 octahedral cations are not homogeneously distributed between the different types of layers.

274 Another factor is cation ordering (cation segregation or dispersion, preferred cation pairs or triads),

275 which modifies the relative proportions of metal-OH groups and can considerably affect the relative

276 intensity of the corresponding infrared bands. Still one more factor is the crystal-chemical

277 environment in the octahedral and tetrahedral sheet around the specific cations-OH groups, which

278 can displace the position of the bands. Bishop et al. (2011) provide an example of the effect of the

279 composition of the tetrahedral sheet. Beyond the above, severe differences of hydration state can

280 also modify OH band positions and intensity (Xu et al., 2000). However, modifications generated

281   beyond the immediate atoms surrounding OH groups are complex, not always consistent and

282   frequently very small (Bishop et al., 2011; Xu et al., 2000). As indicated above, our study was

283   carried out in approximately constant hydration conditions in which smectite layers were hydrated,

284   thus ruling out effects from very contrasting hydration states. Considering all of the above, it is

285   reasonable to attain a first approximation without including less important variables. Given the

286   complexity of the results, the strategy followed here to further investigate connections between the

287   chemistry and NIR spectra of the studied clays was to look for meaningful correlations that can

288   direct the interpretation of the calculated bands.

289

290   The most important factor determining OH band positions is the nature of the cations immediately

291   surrounding OH groups, and thus the analysis was focused on them. Several correlations between

292   normalized NIR band areas and relative proportions of octahedral cations were attempted (Figures

293   3 and 4). First of all, the bands in the spectra were divided into two groups, those from dioctahedral

294   and those from trioctahedral environments. As, typically, trioctahedral clays (i.e., with large Mg +

295   Fe^{2+} content) have the maximum absorption of the investigated band at 2.3 μm or higher

296   wavelength and dioctahedral clays (major Al and Fe^{3+}) below this value, a regression of the

297   normalized area above and below 2.3 μm versus the ratio (Al+Fe^{3+} / Al+Fe^{3+}+Mg+Fe^{2+}) should

298   produce a meaningful correlation. Such is the case for the dioctahedral clays, G-N and nontronites

299   (Figure 3, top row). The G-N and nontronite samples were plotted both separately and together to

300   test whether they would follow a similar trend (Figure 3, top row). They can be considered to fall

301   within the same trend, although the correlation values are lower in the combined plot than in the

302   independent plots. Interestingly, the submarine nontronites appear to be marginally closer to the

303   trend of the G-N samples than Nontronite 33B, which might be due to the greater Mg content of G-

304   N and submarine nontronite specimens (Nontronite 33B is of terrestrial origin). The nontronites are

305   slightly off the trend of the G-N samples probably because the former do not have Fe^{2+}, as the

306   latter do. For the samples with one or two trioctahedral layer components, T-N and T-S, the

307   correlations are not meaningful (Figure 4, top row).

308

309   Secondly, a simplified approach was followed, focused on the main cations only, Fe and Mg. The

310   normalized intensity of the $(Fe^{3+})_2OH$ band versus the ratio (Fe^{3+} / Mg) produces a good correlation

311   for G-N and nontronite samples (Figure 3, middle row). Because in this analysis Fe^{2+} is not

312   considered, the G-N and nontronite specimens come closer into the same trend (Figure 3, panel

313   G-N, Nont). The T-N samples show a meaningful correlation with this approach, although this

314   correlation arises mainly from the one data point in the bottom, left corner (Figure 4, T-N in the

315   middle row). The T-S samples do not produce a meaningful correlation (Figure 4, middle row,

316   right).

317

318   Finally, the complementary approach was followed, plotting the normalized area of the main Mg

319   band (FeOHMg for the G-N, nontronite and T-N groups; the two talc Mg_3OH bands for the T-S

320   group; all versus $Mg / Mg+Fe^{3+}$; Table 2). Again, the dioctahedral samples develop meaningful

321   correlations (Figure 3, bottom row) but T-N and T-S samples do not (Figure 4, bottom row). It can

322   be argued that the analysis of T-S samples that do not use Fe^{2+}, as in the two bottom T-S plots of

323   Figure 4, is incorrect, because octahedral Fe^{2+} is as abundant as Fe^{3+} in these samples (Table 1).

324   However, using Fe^{2+} did not improve results (Figure 4, top T-S plot). Overall, the best correlations

325   for the dioctahedral samples are those considering Mg, rather than Fe. Based on these

326   observations, it is probably a good strategy to use the cation with the second greatest octahedral

327   concentration, rather than the most abundant, to investigate the contribution to IR absorption of the

328   several bands. The reason is because there is greater probability for the second most abundant

329   cation to generate one single band, which decreases the error in the band identification and

330   quantification. The most abundant cation has a greater probability to contribute to several bands,

331   resulting in larger uncertainty in the identification and calculations.

332

333   From the above analysis, it appears that Fe/Mg-rich clays of a dioctahedral nature generate NIR

334   bands in the 2.1-2.35 μm region that can be correlated well with their octahedral chemistry,

335   although details regarding the intensity and position of these bands may not match the octahedral

336   composition. Reasons for these differences have been suggested above. Mixed-layer clays with

337 one or two trioctahedral components, however, do not produce 2.1-2.35 μm NIR bands that can be

338 correlated with their octahedral chemistry. Clays from the T-N group produce some trends that may

339 be useful, but the T-S samples do not. The possible reason for this different behaviour between di-

340 and trioctahedral clays is discussed below. A structural complication exists for the T-N samples

341 indicated by Cuadros et al. (2013b), consisting in the fact that talc layers have nontronite domains

342 within their octahedral sheet. This can cause irregularities in the distribution of the cations and the

343 types of metal groups they produce around hydroxyls, because dioctahedral Fe-rich domains are

344 present in trioctahedral Mg-rich sheets.

345

346 The nature of the two OH bands in the NIR spectrum at ~1.4 and 2.18-2.35 μm has been

347 determined as corresponding to the first overtone of the fundamental OH stretching band and a

348 combination of the OH stretching and bending bands, respectively (e.g., Bishop et al., 2002b), both

349 in the mid-IR. This can be shown by compiling and averaging values of the center of OH stretching

350 and bending bands for different cation groups, calculating the position of the corresponding

351 overtone and combination bands and comparing them with experimental values (Table 3). The first

352 overtone of the OH stretching vibration does not appear exactly at twice the value of the

353 fundamental band, but slightly below, due to the anharmonic character of the OH vibration. The

354 approximate value of 1.96 was used here for the calculation of the first overtone, following Bishop

355 et al., (2002b). The combination of bending and stretching vibrations is calculated as the sum of

356 the wavenumbers of both vibrations. The agreement between the calculated and experimental

357 values is very good (Table 3).

358

359 Thus, the position of the combination band at 2.1-2.35 μm in the NIR is controlled by the position of

360 the OH stretching and bending bands in the mid-IR. For dioctahedral clays, substitution of Mg or

361 Fe for Al displaces the position of OH bands, both stretching and bending, towards lower

362 wavenumbers (Figure 5, Table 3). Thus the displacements of the stretching and bending bands are

363 in the same direction and, when the wavenumber values are added, both contribute to modify the

364 position of the combination NIR band in the same direction. In trioctahedral phyllosilicates,

365 however, the opposite is true. Substitution of Al or Fe^{3+} for Mg in the octahedral sheet displaces the

366 stretching and bending OH mid-IR bands in opposite directions (Figure 5, Table 3). As a result, the

367 contribution of both vibrations to the combination band in the NIR displaces its position in the

368 opposite direction, partially or totally cancelling each other. This is probably the reason why there is

369 such a poor correlation between octahedral chemistry and the relative intensity of individual NIR

370 components in the samples with trioctahedral layers.

371

372 **Implications**

373 The analysis performed here probably cannot be carried out on Martian orbital spectra because

374 they may be too noisy to allow decomposition with sufficient detail. However, this analysis

375 produces information of great interest for their interpretation. The normalized intensity of individual

376 components of the NIR OH combination band of dioctahedral 2:1 phyllosilicates is correlated with

377 the chemistry of the octahedral sheet to such an extent that it should allow a good prediction of the

378 octahedral composition based on the overall band center, as shown by Michalski et al. (2014) for

379 the samples studied here. The two fundamental vibrations combining to produce the NIR

380 combination band, OH stretching and OH bending, both in the mid-IR region, have their position

381 modified by the octahedral chemistry in a consistent and constructive way, resulting in a well-

382 developed trend between chemistry and band location. This correlation should be exploited in the

383 analysis of 2:1 dioctahedral phyllosilicates on Mars. Moreover, kaolinite, although a 1:1 clay

384 mineral, could also be included in this type of analysis because (1) the position of its OH

385 combination band falls within the same trend as that of the 2:1 dioctahedral clays, (2) some

386 octahedral substituion is possible in kaolinite, and (3) kaolinite-smectite mixed-layer, which has

387 octahedral sheets of intermediate composition, is also present on Mars (Cuadros and Michalski,

388 2013).

389

390 Alterations to the trend between octahedral chemistry and position of the OH combination band in

391 the 2.18-2.35 μm range for dioctahedral phyllosilicates may arise due to different cation

392 distributions. Random distribution, cation segregation, cation dispersion, existence of preferred

393 pairs and of excluded pairs, all of them produce distributions of individual OH absorption bands

394   with different relative intensities, which affects the position of the overall band. Octahedral cation

395   distribution is worth investigating on Mars because cation ordering is probably related to the

396   environment and mechanism of the phyllosilicate formation.

397

398   In trioctahedral 2:1 phyllosilicates, however, it is problematic to assess their octahedral

399   composition solely from the location of the OH combination band at ~2.3 μm because the two

400   corresponding fundamental bands are displaced in the opposite direction by the same octahedral

401   substitutions. The result is a null or inconsistent effect of such substitutions on the band position.

402   Thus, on Mars, spectra that are interpreted as saponite may in fact correspond to phyllosilicates

403   with significant Fe^{3+} or Fe^{2+} octahedral substitution (Figure 6), with or without mixed-layer phases.

404

405   Interestingly, the clay investigated by Curiosity at the floor of Gale Crater is an Fe-rich saponite

406   (Vaniman et al., 2014; Bristow et al., 2015). Based on our conclusions, it might be difficult to relate

407   NIR and chemical data for clays of this or similar crystal-chemistry. In order to avoid the uncertainty

408   generated by this situation, it is advisable to investigate also the first overtone of the stretching OH

409   vibration at ~1.4 μm. In this band, the position is only controlled by the displacements of one

410   fundamental vibration. Unfortunately, there are several problems with the analysis of this band. In

411   the first place, the 1.4 μm band has a reduced response to clay chemistry (total range of variation

412   of 0.023 μm in Table 3, as opposed to a 0.148 μm range for the OH combination band). In the

413   second place, this band has frequently low intensity, as observed in clays from Earth (Figure 1)

414   and Mars (Arvidson et al., 2014). The reasons for this low intensity are unclear so far, but may be

415   related to crystal-chemical order. Loss of hydration water alone, as suggested by Arvidson et al.

416   (2014), is not a possible reason because this band is generated by structural OH groups (the

417   molecular water component in the range 1.41-1.45 has a limited contribution as shown by Bishop

418   et al., 1994) . However, if the above problems can be overcome, the 1.4 μm band can be a useful

419   tool to investigate the chemistry of trioctahedral clays. First, the general trioctahedral character of

420   the clay can be ascertained from the position of the combination OH band at ~2.3 μm. Second, one

421   can search for displacements of the 1.4 μm towards higher frequency (lower wavenumber, Figure

16

422   5) that may indicate Fe^{3+} and Al substitution. Further investigation of the crystal-chemical controls

423   on the position and intensity of the 1.4 μm band will help characterization of Martian clays.

424

425   Acknowledgements

430

431   References

433   Arvidson, R.E. et al. (2014) Ancient aqueous environments at Endeavour Crater, Mars. Science,
434   343, 1248097.

436   Bibring, J.-P. et al. (2005) Mars surface diversity as revealed by the OMEGA/Mars Express
437   observations. Science, 307, 1576-1581.

439   Bibring, J.-P. et al. (2006) Global mineralogical and aqueous Mars history derived from
440   OMEGA/Mars Express data. Science, 312, 400-404.

442   Bishop, J., Pieters, C., Edwards, J. (1994) Infrared spectroscopic analyses on the nature of water in
443   montmorillonite. Clays and Clay Minerals, 42, 702-716.

445   Bishop, J., Madejová, J., Komadel, P., and Fröschl. H. (2002a) The influence of structural Fe, Al and
446   Mg on the infrared OH bands in spectra of dioctahedral smectites. Clay Minerals, 37, 607-616.

448   Bishop, J., Murad, E., and Dyar, M. (2002b) The influence of octahedral an tetrahedral cation
449   substitution on the structure of smectites and serpentines as observed through infrared
450   spectroscopy. Clay Minerals, 37, 617-628.

452   Bishop, J., Lane, M., Dyar, M.D., and Brown, A. (2008) Reflectance and emission spectroscopy
453   study of four groups of phyllosilicates: smectites, kaolinite-serpentines, chlorites and micas. Clay
454   Minerals, 43, 35-54.

456   Bishop, J., Gates, W., Makarewicz, H., McKeown, N., and Hiroi, T. (2011) Reflectance spectroscopy
457   of beidellites and their importance for Mars. Clays and Clay Minerals, 59, 378-399.

459   Bristow, T. et al. (2015) The origin and implications of clay minerals from Yellowknife Bay, Gale
460   crater, Mars. American Mineralogist, 100, 824-836.

462   Burns, R.G. (1993) Rates and Mechanisms of Chemical-Weathering of ferromagnesian silicate
463   minerals on Mars. Geochimica et Cosmochimica Acta, 57, 4555-4574.

465   Carr, M.H. (1996) Water on Mars, 228 p. Oxford University Press, USA.

467   Carter, J., Poulet, F., Bibring, J.-P., Mangold, N., and Murchie, S. (2013) Hydrous minerals on Mars
468   as seen by the CRISM and OMEGA imaging spectrometers: Updated global view. Journal of
469   Geophysical Research: Planets, 118, 831–858. doi:10.1029/2012JE004145

471   Cuadros, J., and Michalski, J.R. (2013) Investigation of Al-rich clays on Mars: evidence for kaolinite-
472   smectite mixed-layer versus mixture of end-member phases. Icarus, 222, 296-306.

474   Cuadros, J., Dekov, V., and Fiore, S. (2008) Crystal-chemistry of the mixed-layer sequence talc–talc-
475   smectite–smectite from submarine hydrothermal vents. American Mineralogist, 93, 1338-1348.

477   Cuadros, J., Afsin, B., Jadubansa, P., Ardakani, M., Ascaso, C., and Wierzchos, J. (2013a) Microbial
478   and inorganic control on the composition of clay from volcanic glass alteration experiments.
479   American Mineralogist, 98, 319-334.

480

481 Cuadros, J., Michalski, J.R., Dekov, V., Bishop, J., Fiore, S., and Dyar, M.D. (2013b) Crystal-chemistry
482 of interstratified Mg/Fe-clay minerals from seafloor hydrothermal sites. Chemical Geololgy, 360-
483 361, 142-158. http://dx.doi.org/10.1016/j.chemgeo.2013.10.016.

484

485 Dainyak, L., Drits, V., Zviagina, B., and Lindgreen, H. (2006) Cation redistribution in the octahedral
486 sheet during diagenesis of illite-smectites from Jurassic and Cambrian oil source rock shales.
487 American Mineralogist, 91, 589-603.

488

489 Di Leo, P., and Cuadros, J. (2003) ^{113}Cd, ^{1}H NMR and FTIR analysis of Cd^{2+} adsorption on
490 dioctahedral and trioctahedral smectite. Clays and Clay Minerals, 51, 403-414.

491

492 Douglas, S., and Beveridge, T. (1998) Mineral formation by bacteria in natural microbial
493 communities. FEMS Microbiology Ecology, 26, 79-88.

494

495 Ehlmann, B.L. et al. (2011a) Subsurface water and clay mineral formation during the early history
496 of Mars. Nature, 479, 53-60.

497

498 Ehlmann, B.L., Mustard, J.F., Clark, R.N., Swayze, G.A., and Murchie, S.L. (2011b) Evidence for low-
499 grade metamorphism, hydrothermal alteration, and diagenesis on Mars from phyllosilicate
500 mineral assemblages. Clays and Clay Minerals, 59, 359-377.

501

502 Fialips, C.-I., Huo, D., Yan, L., Wu, J., and Stucki, J. (2002) Infrared study of reduced and reduced-
503 reoxidized ferruginous smectite. Clays and Clay Minerals, 50, 455-469.

504

505 Grauby, O., Petit, S., Decarreau, A., and Baronnet, A. (1994) The nontronite-saponite series: An
506 experimental approach. European Journal of Mineralogy, 6, 99-112.

507

508 Kloprogge, J.T., and Frost, R.L. (2001) Infrared emission spectroscopic study of the dehydroxylation
509 of some natural and synthetic saponites. Neues Jahrbuch für Mineralogie-Monatshefte, 10, 446-
510 463.

511

512 Madejová, J., and Komadel, P. (2001) Baseline studies of the Clay Minerals Society Source Clays:
513 Infrared methods. Clays and Clay Minerals, 49, 410-432.

514

515 Madejová, J., Komadel, P., and Čičel, B. (1994) Infrared study of octahedral site populations in
516 smectites. Clay Minerals, 29, 319-326.

517

518 Malla, P.B., and Komarneni, S. (1993) Properties and characterization of Al$_2$O$_3$ and SiO$_2$-TiO$_2$
519 pillared saponite. Clays and Clay Minerals, 41, 472-483.

520

521 McKeown, N.K., Bishop, J.L., Cuadros, J., Hillier, S., Amador, E., Makarewicz, H.D., Parente, M., and
522 Silver, E.A. (2011) Interpretation of reflectance spectra of clay mineral-silica mixtures: implications
523 for Martian clay mineralogy at Mawrth Vallis. Clays and Clay Minerals, 59, 400-415. doi
524 10.1346/CCMN.2011.0590404

525

526 Michalski, J.R., Cuadros, J., Dekov, V., Bishop, J.L., Fiore, S., and Dyar, M.D. (2014) Constraints on
527 the crystal chemistry of Fe-Mg clays on Mars based on infrared analyses of Fe-rich seafloor clays.
528 45th Lunar and Planetary Science Conference, Houston, USA. Abstract 1781.

529

530   Murchie, S. et al. (2009) A synthesis of Martian aqueous mineralogy after 1 Mars year of
531   observations from the Mars Reconnaissance Orbiter. Journal of Geophysical Research, 114,
532   E00D06.

533

534   Neumann, A., Petit, S., and Hofstetter, T. (2011) Evaluation of redox-active iron sites in smectites
535   using middle and near infrared spectroscopy. Geochimica et Cosmochimica Acta, 75, 2336-2355.

536

537   Parente, M., Makarewicz H.D., and Bishop, J.L. (2011) Decomposition of mineral absorption bands
538   using nonlinear least squares curve fitting: Application to Martian meteorites and CRISM data.
539   Planetary and Space Science, 59, 423–442.

540

541   Petit, S., Decarreau, A., Martin, F., and Buchet, R. (2004) Refined relationship between the position
542   of the fundamental OH stretching and the first overtones for clays. Physics and Chemistry of
543   Minerals, 31, 585-592.

544

545   Post, J.L. (1984) Saponite from near Ballarat, California. Clays and Clay Minerals, 32, 147-153.

546

547   Poulet, F. et al. (2005) Phyllosilicates on Mars and implications for the early Mars history. Nature,
548   438, 632-627.

549

550   Robertson, K.M., and Milliken, R.E. (2014) Spectroscopic laboratory evidence for iron reduction in
551   phyllosilicates under low pressure conditions. 45th Lunar and Planetary Science Conference.
552   Abstract 1895.

553

554   Vaniman et al. (2014) Mineralogy of a mudstone at Yellowknife Bay, Gale Crater, Mars. Science,
555   343, 1243480.

556

557   Walter, M.R., and Des Marais, D.J. (1993) Preservation of biological information in thermal spring
558   deposits: developing a strategy for the search for fossil life on Mars. Icarus, 101, 129-143.

559

560   Wilkins, R., and Ito, J. (1967) Infrared spectra of some synthetic talcs. American Mineralogist, 52,
561   1649-1661.

562

563   Xu, W., Johnston, C.T., Parker, P., and Agnew, S.F. (2000) Infrared study of water sorption on Na-,
564   Li-, Ca- and Mg-exchanged (SWy-1 and SAz-1) montmorillonite. Clays and Clay Minerals, 48, 120-
565   131.

566

567   Zhang, M., Hui, Q., Lou, X.-J., Redfern, S., Salje, E., and Tarantino, S. (2006) Dehydroxylation,
568   proton migration, and structural changes in heated talc: An infrared spectroscopic study. American
569   Mineralogist, 91, 816-825.

570

571   Zviagina, B., McCarty, D., Środoń, J., and Drits, V. (2004) Interpretation of infrared spectra of
572   dioctahedral smectites in the region of OH-stretching vibrations. Clays and Clay Minerals, 52, 399-
573   410.

574

575

576

577

578 Table 1. Octahedral composition of the studied samples (Cuadros et al., 2013b). The mineral phases and
579 percent of smectite (Di- and Tri-sm are dioctahedral and trioctahedral smectite) are added for reference. G-
580 N: glauconite-nontronite mixed-layer; N: nontronite; T-N: talc-nontronite mixed-layer; T-S: talc-saponite
581 mixed-layer.

	Sample	Min	% Di-sm	% Tri-sm	Al oct	Mg	Fe III	Fe II	Mn	Ti	Sum oct
DIOCTAHEDRAL	Va22..1144-1145	G-N	68		0.00	0.25	1.69	0.05	0.00	0.00	2.00
	Va22..612-614	G-N	59		0.02	0.20	1.79	0.00	0.00	0.00	2.02
	Va22..588-591	G-N	56		0.05	0.17	1.73	0.04	0.00	0.00	1.99
	Va22..603-604	G-N	50		0.03	0.18	1.79	0.00	0.00	0.00	2.00
	Va22..1145-1146	G-N	47		0.04	0.25	1.65	0.05	0.00	0.00	1.99
	Va22..586-587	G-N	39		0.02	0.18	1.83	0.04	0.00	0.00	2.08
	Va22..639-640	G-N	33		0.00	0.23	1.84	0.00	0.00	0.00	2.08
	Va22..1030-1034	G-N	23		0.06	0.17	1.58	0.11	0.05	0.00	1.98
	1183-15	N	100		0.00	0.31	1.67	0.00	0.01	0.00	1.99
	Cy-82-14-5	N	100		0.00	0.28	1.76	0.00	0.00	0.00	2.04
	Nontronite 33B	N	100		0.09	0.03	1.88	0.00	0.00	0.00	2.00
DI-TRI	Va3..150-153	T-N	80		0.00	0.55	1.68	0.07	0.02	0.00	2.33
	Nontronite 51	T-N	76		0.00	0.82	1.09	0.15	0.00	0.01	2.08
	Va22..471-475	T-N	75		0.14	0.15	1.69	0.20	0.01	0.01	2.21
	Va22..575-577	T-N	71		0.03	0.18	1.92	0.00	0.00	0.00	2.13
	Va22..583-586	T-N	69		0.05	0.18	1.96	0.00	0.00	0.01	2.21
	CHN..290-292	T-N	68		0.00	0.18	1.81	0.20	0.08	0.01	2.28
	Va22..602-603	T-N	60		0.00	0.28	1.97	0.00	0.01	0.01	2.27
TRIOCTAHEDRAL	Va3..382-389	T-S		90	0.00	2.03	0.51	0.18	0.00	0.01	2.73
	Sea Cliff Dive	T-S		27	0.06	2.58	0.05	0.29	0.00	0.00	2.99
	POS..155-158	T-S		27	0.00	2.95	0.03	0.03	0.00	0.00	3.01
	Turtle pits	T-S		21	0.00	2.80	0.03	0.20	0.00	0.00	3.03
	POS..56-57	T-S		20	0.00	2.82	0.07	0.05	0.00	0.01	2.96
	POS..31-32	T-S		17	0.00	2.94	0.04	0.02	0.00	0.00	3.00
	POS..140-141	T-S		16	0.00	2.96	0.03	0.02	0.00	0.00	3.01
	POS..113-114	T-S		13	0.00	2.95	0.03	0.02	0.00	0.00	3.00
	Logatchev-2	T-S		11	0.00	2.78	0.10	0.00	0.01	0.00	2.90
	POS..20-21	T-S		10	0.00	2.92	0.03	0.02	0.00	0.00	2.98
	POS..72-73	T-S		6	0.00	3.01	0.01	0.01	0.00	0.00	3.04
	1183-9	T-S		2	0.00	1.52	0.75	0.55	0.01	0.00	2.83

582

583

Sample	Type	% Sm	Pos	Area	Assgn	Pos	Area	Assgn	Pos	Area	Assgn	Pos	Area	Assgn	Pos	Area	Assgn	Pos	Area	Assgn
Va22-1144-1145	G-N	68				2.299	0.497	Fe_2	2.312	0.429	FeMg	2.361	0.073	Fe_3 (+2)						
Va22-612-614	G-N	59				2.295	0.804	Fe_2	2.318	0.105	FeMg	2.358	0.090	Fe_3 (+2)						
Va22-588-591	G-N	56				2.295	0.792	Fe_2	2.318	0.111	FeMg	2.359	0.097	Fe_3 (+2)						
Va22-603-604	G-N	50				2.295	0.777	Fe_2	2.318	0.108	FeMg	2.362	0.115	Fe_3 (+2)						
Va22-1145-1146	G-N	47	2.281	0.082	Fe_2 (sm?)	2.297	0.426	Fe_2 (glc?)	2.313	0.527	FeMg	2.364	0.047	Fe_3 (+2)						
Va22-586-587	G-N	39				2.294	0.826	Fe_2	2.318	0.087	FeMg	2.361	0.087	Fe_3 (+2)						
Va22-639-640	G-N	33	2.272	0.147	Fe_2 (sm?)	2.295	0.530	Fe_2 (glc?)	2.316	0.229	FeMg	2.356	0.094	Fe_3 (+2)						
Va-22-1030-1034	G-N	23				2.298	0.595	Fe_2	2.319	0.166	FeMg	2.358	0.238	Fe_3 (+2)						
1183-15	N	100							2.286	0.230	Fe_2 (+3)	2.304	0.770	FeMg						
Cy-82-14-5	N	100							2.283	0.151	Fe_2 (+3)	2.302	0.826	FeMg	2.329	0.023	Mg_3 / Mg_2Fe			
Nontronite 33B	N	100	2.204	0.015	Al_2	2.239	0.005	AlFe	2.286	0.980	Fe_2 (+3)									
Va3-150-153	T-N	80							2.280	1.000	Fe_2 (+3)									
Nontronite 51	T-N	76	2.203	0.008	Al_2?	2.243	0.057	AlFe?	2.287	0.849	Fe_2 (+3)	2.316	0.080	FeMg / Mg_3	2.354	0.006	Mg_3 / Fe_3(+2)			
Va22-471-475	T-N	75							2.295	0.949	Fe_2 (+3)	2.316	0.051	FeMg / Mg_3						
Va22-575-577	T-N	71							2.292	1.000	Fe_2 (+3)									
Va22-583-586	T-N	69							2.292	0.986	Fe_2 (+3)	2.324	0.014	Mg_3 / Mg_2Fe						
CHN-290-292	T-N	68							2.292	1.000	Fe_2 (+3)									

Table 2. Position, relative area (normalized to 1) and possible assignment of the components resulting from the curve fitting calculations of NIR spectra. The nature of the samples (type column) and % smectite layers are included for reference. In some cases two possible assignments are proposed. Question marks indicate tentative assignments or open questions.

22

Name																				
Va22-602-603	T-N	60							2.292	1.000	Fe$_2$ (+3)									
Va3-382-389	T-S	90	2.195	0.060	AlMg?				2.264	0.137	Fe$_2$ (+?)	2.287	0.294	Mg$_3$ talc	2.314	0.509	Mg$_3$ talc			
Sea Cliff Dive	T-S	27				2.234	0.012	AlFe	2.279	0.095	Fe$_2$ (+?)	2.291	0.155	Mg$_3$ talc	2.314	0.725	Mg$_3$ talc	2.352	0.012	Fe$_3$(2+)/ Mg$_3$ sm
POS 155-158	T-S	27	2.220	0.030	AlMg				2.271	0.068	Fe$_2$ (+?)	2.287	0.239	Mg$_3$ talc	2.310	0.664	Mg$_3$ talc			
Turtle pits	T-S	21				2.233	0.010	AlFe	2.283	0.102	Fe$_2$ (+?)	2.292	0.178	Mg$_3$ talc	2.314	0.710	Mg$_3$ talc			
POS 56-57	T-S	20							2.275	0.083	Fe$_2$ (+?)	2.287	0.218	Mg$_3$ talc	2.310	0.700	Mg$_3$ talc			
POS 31-32	T-S	17				2.223	0.027	AlFe	2.273	0.095	Fe$_2$ (+?)	2.287	0.218	Mg$_3$ talc	2.310	0.659	Mg$_3$ talc			
POS 140-141	T-S	16	2.216	0.065	AlMg				2.269	0.081	Fe$_2$ (+?)	2.286	0.228	Mg$_3$ talc	2.310	0.626	Mg$_3$ talc			
POS 113-114	T-S	13				2.222	0.040	AlFe	2.270	0.060	Fe$_2$ (+?)	2.287	0.248	Mg$_3$ talc	2.310	0.651	Mg$_3$ talc			
Logatchev-2	T-S	11	2.211	0.024	AlMg	2.229	0.031	AlFe	2.280	0.140	Fe$_2$ (+?)	2.291	0.180	Mg$_3$ talc	2.312	0.621	Mg$_3$ talc	2.352	0.005	Fe$_3$(2+)/ Mg$_3$ sm
POS 20-21	T-S	10				2.228	0.145	AlFe	2.270	0.110	Fe$_2$ (+?)	2.286	0.230	Mg$_3$ talc	2.310	0.660	Mg$_3$ talc			
POS 72-73	T-S	6				2.231	0.035	AlFe	2.270	0.094	Fe$_2$ (+?)	2.286	0.244	Mg$_3$ talc	2.310	0.663	Mg$_3$ talc			
1183-9	T-S	2							2.274	0.034	Fe$_2$ (+?)	2.293	0.19	Mg$_3$ talc	2.318	0.777	Mg$_3$ talc			

584   sm: smectite; glc: glauconite.

23

585

586

587 Table 3. Experimental and calculated values of the location of several OH bands in the mid- and near-infrared. The location of the fundamental stretching and
588 bending bands are used to calculate those of the first stretching overtone and the bending plus stretching combination.

	Stretching		Stretch. overtone		Bending		Bend + stretch			Stretch. overtone	Bend + stretch
	Experimental		Calculated^a		Experimental		Calculated^b			Experimental	Experimental
	cm^{-1}	µm	cm^{-1}	µm	cm^{-1}	µm	cm^{-1}	µm		µm	µm
Al$_2$OH Beid	3628^c	2.756	7111	1.406	942^d	10.616	4570	2.188	Beid	1.399 – 1.412^e	2.180 – 2.190^e
Al$_2$OH Mont	3628^c	2.756	7111	1.406	915^f	10.929	4543	2.201	Mont	1.412 – 1.414^g	2.205 – 2.210^g
AlMgOH	3608^h	2.772	7072	1.414	842^f	11.877	4450	2.247			
AlFeOH	3584^h	2.790	7025	1.424	876^f	11.416	4460	2.242			
MgFeOH	3572^i	2.700	7001	1.428	775^f	12.903	4347	2.300			
Fe$_2$OH	3553^h	2.815	6964	1.436	820^j	12.195	4373	2.287	Nont	1.410 – 1.466^g	2.235 – 2.286^g
Mg$_3$OH	3684^k	2.714	7221	1.385	664^l	15.060	4348	2.300	Tri-sm	1.391^m	2.310^m
									Talc	1.392^n	2.313^n
Mg$_2$FeOH	3661°	2.732	7174	1.394					Talc	1.397^p	
MgFe$_2$OH	3644°	2.744	7142	1.400					Talc	1.401^p	
Fe$_3$OH	3621^q	2.762	7097	1.409	646^r	15.480	4267	2.344	Tri-sm		2.353^r
									Talc	1.405^s	

589 ^{a} Wavenumber of stretching overtone = Wavenumber of stretching × 1.96.
590 ^{b} Wavenumber = wavenumber of stretching + wavenumber of bending.
591 ^{c} Averaged from values in Madejová et al. (1994) using the individual decomposed bands, and Bishop et al. (2002a) using the overall bands in Al-rich smectites.
592 ^{d} Averaged from values in Bishop et al. (2011).
593 ^{e} Range from Bishop et al. (2011).
594 ^{f} Averaged from values in Bishop et al. (2002a).
595 ^{g} Range from Bishop et al. (2002b).
596 ^{h} Averaged from values in Madejová et al. (1994; excluding AlMgOH-assigned band at 3684 cm^{-1}), Fialips et al. (2002), Zviagina et al.(2004), Dainyak et al. (2006).

24

597   [i] Averaged from values in Madejová et al. (1994), Fialips et al. (2002), Zviagina et al.(2004).
598   [j] Averaged from values in Bishop et al. (2002a), Fialips et al. (2002).
599   [k] Averaged from Bishop et al. (2002b) and Di Leo and Cuadros (2003) from saponite, and Petit et al. (2004) from talc.
600   [l] Averaged saponite values from Kloprogge and Frost (2001), Grauby et al. (1994), Bishop et al. (2008).
601   [m] Values for hectorite from Madejová and Komadel (2001).
602   [n] Values for talc from Zhang et al. (2006).
603   [o] Averaged from several values of talc and talc-saponite from Cuadros et al. (2008), Petit et al. (2004), Wilkins and Ito (1967).
604   [p] From Petit et al. (2004).
605   [q] Averaged from talc values in Petit et al. (2004), Wilkins and Ito (1967), and from smectite values in Neumann et al. (2011).
606   [r] From Neumann et al. (2011).
607   [s] From Petit et al. (2004).
608
609

610

611   Figures

612

613   Figure 1. Near-infrared spectra representative of the several groups of samples investigated. T-S:

614   talc-saponite mixed-layer; T-N: talc-nontronite; N: nontronite; G-N: glauconite-nontronite.

615

616   Figure 2. Results of band decomposition for two of the samples. The band on the far right is not

617   part of the OH system. The grey, smooth line is the overall modeled spectrum, which coincides

618   exactly with some of the individual bands in some areas. T-S: talc-saponite mixed-layer.

619

620   Figure 3. Correlations between the normalized intensities of individual decomposed NIR bands and

621   octahedral cation ratios. The top row uses all bands and all cations. The other two rows focus the

622   analysis on the main bands and most abundant cations. Nontronite (N) and glauconite-nontronite

623   (G-N) bands are plotted together in the right-hand side panels. The dash lines are for regressions

624   including Nontronite 33B, a non-marine specimen. The solid lines include only the marine samples.

625

626   Figure 4. Correlations between the normalized intensities of individual decomposed NIR bands and

627   octahedral cation ratios. As in Figure 3, the top row uses all bands and all cations; whereas the

628   other two rows focus the analysis on the main bands and most abundant cations. Talc and

629   saponite have a Mg_3OH component at ~2.29 μm (Table 2), which was computed with the bands

630   above 2.30 μm. T-N: talc-nontronite mixed-layer; T-S: talc-saponite.
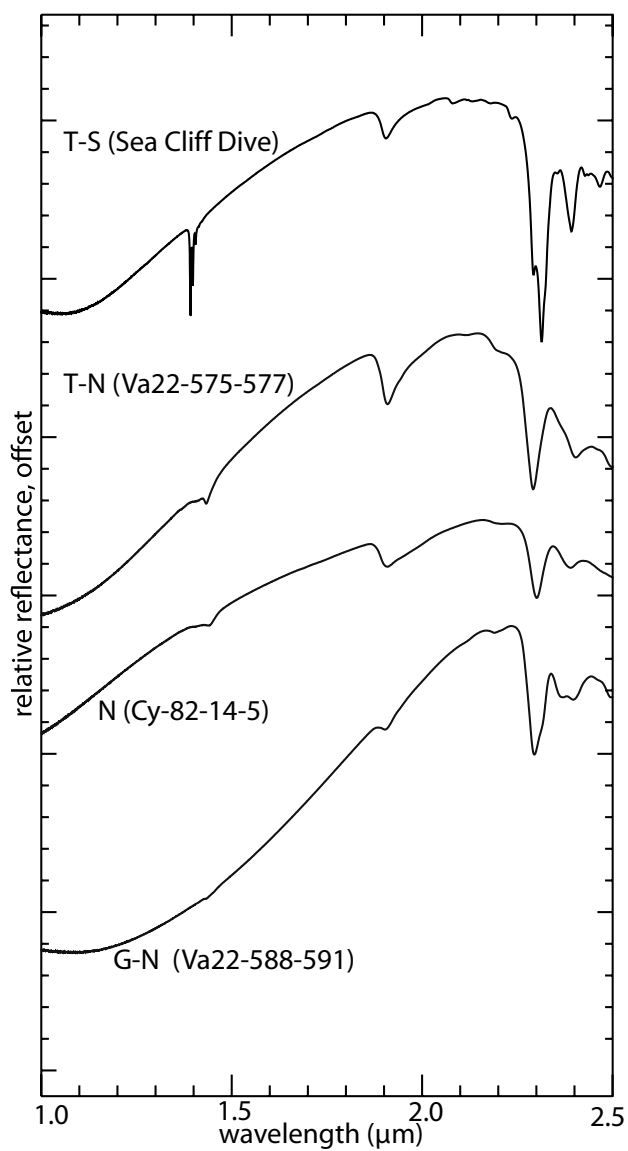
631

632   Figure 5. Effect of cation substitution on OH band location. Sketch indicating how the increasing

633   proportion of the several octahedral cations modifies the position of the OH stretching (left) and

634   bending vibrations (right) in dioctahedral and trioctahedral 2:1 clays. Arrows indicate the direction

635   of change produced by each cation. The length of the arrows is an indication of the extent of the

636   change. For dioctahedral phyllosilicates, the cations produce changes of the position of OH

637   stretching and bending vibrations in the same direction. In trioctahedral clays Mg, Al and Fe(III)

638   produce changes in the opposite direction in OH stretching and bending vibrations.

639

640   Figure 6. Comparison of the ~2.31 μm band of one of the saponites in the CRISM library and three

641   of our samples, corresponding to T-S (talc-smectite) of variable smectite and octahedral Fe

642   contents. LASA51 (or SapCa-1) has reported octahedral compositions in the ranges 2.61-2.87 Mg,

643   0.03-0.09 Fe, 0.00-0.15 Al per $O_{10}(OH)_2$ (Post, 1984; Malla and Komarneni, 1993); Sea Cliff Dive has

644   0.05 octahedral Fe(III) and 0.29 Fe(II); Logatchev-2 has 0.10 Fe(III); 1183-9 has 0.75 Fe(III) and 0.55

645   Fe(II). See Table 1 for complete octahedral compositions.
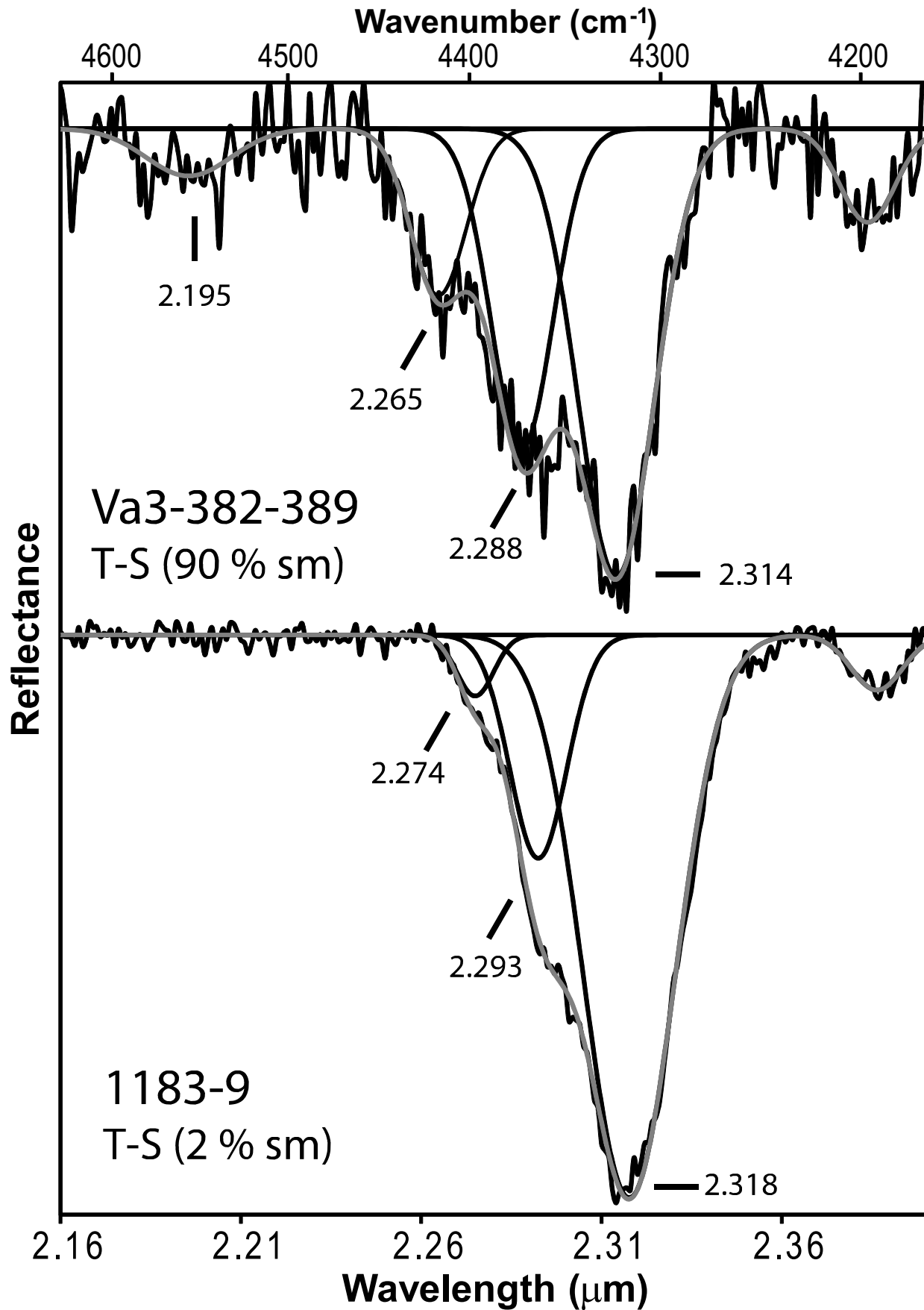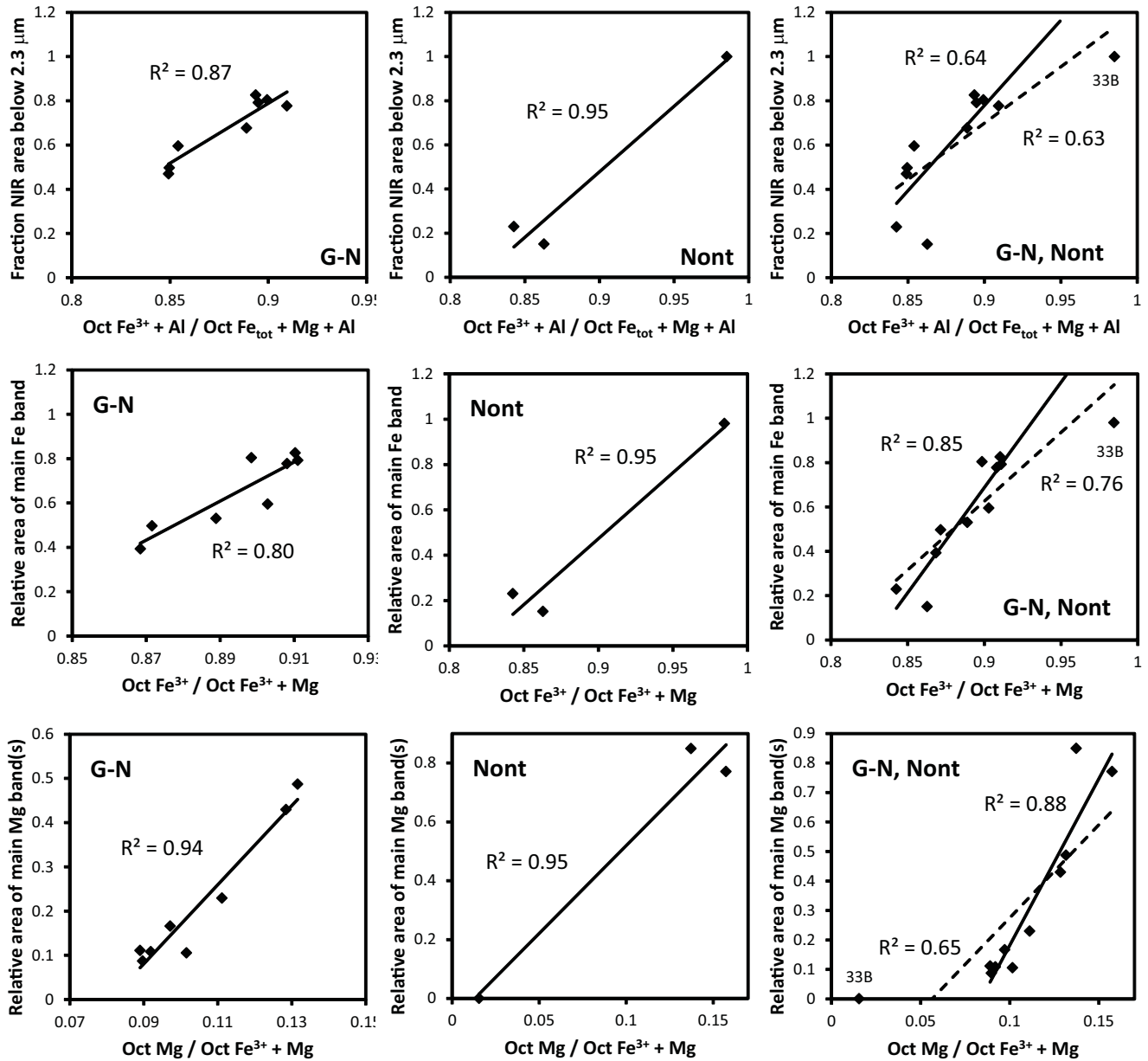
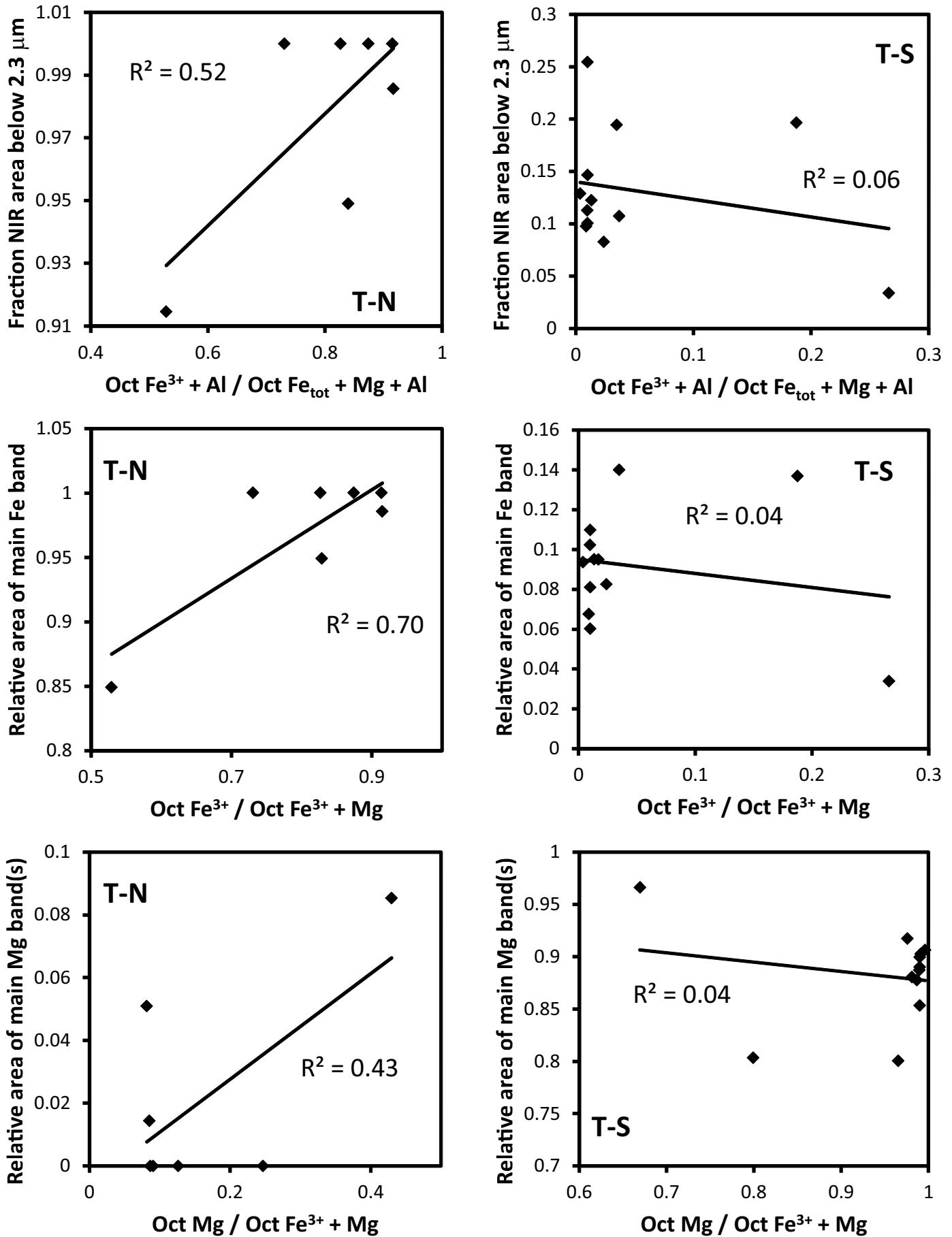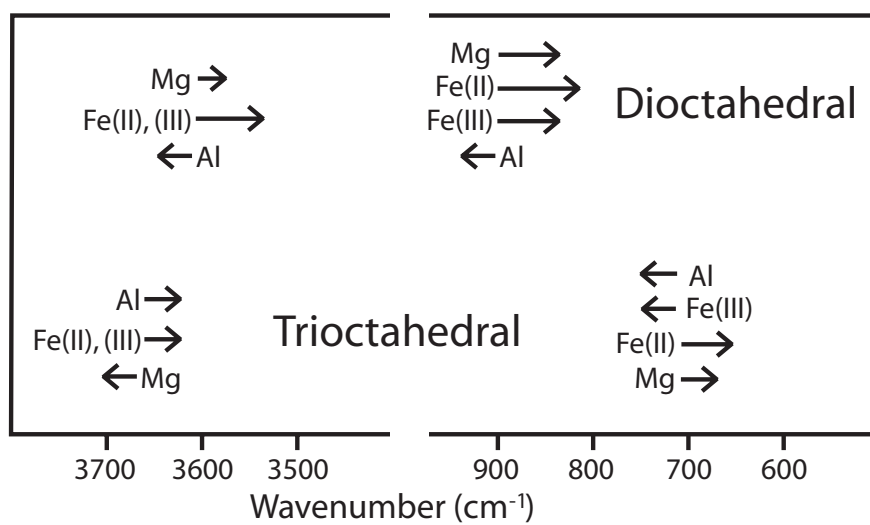FIGURE 1

Figure 2

Figure 3

Figure 4

Fig. 5

FIGURE 6